Autofocus algorithm for dispersion correction in optical coherence tomography

Daniel L. Marks, Amy L. Oldenburg, J. Joshua Reynolds, and Stephen A. Boppart

Practical clinical optical coherence tomography (OCT) systems require automatic tools for identifying and correcting flaws in OCT images. One type of flaw is the loss of image detail owing to the dispersion of the medium, which in most cases is unknown. We present an autofocus algorithm for estimating the delay line and material dispersion from OCT reflectance data, integrating a previously presented dispersion compensation algorithm to correct the data. The algorithm is based on minimizing the Renyi entropy of the corrected axial-scan image, which is a contrast-enhancement criterion. This autofocus algorithm can be used in conjunction with a high-speed, digital-signal-processor-based OCT acquisition system for rapid image correction. © 2003 Optical Society of America

OCIS codes: 100.3010, 110.4500, 260.2030.

1. Introduction

Optical coherence tomography (OCT) is rapidly becoming a practical diagnostic clinical instrument. Its high resolution surpasses other noninvasive three-dimensional imaging modalities, including x-ray computed tomography, magnetic resonance imaging, and ultrasound imaging, making it suitable for *in vivo* analysis at near histological resolutions. For OCT technology to achieve the utility of other imaging systems, it is necessary to develop the system that is usable by personnel outside the field of optical engineering. Because numerous problems can compromise imaging performance, it is highly desirable to build these systems with as much automatic analysis as possible to compensate for these problems. Dispersion, which can corrupt the resolution of the images, can be problematic because it depends on the material or materials the light passes through, which are not necessarily known *a priori*. Fortunately, dispersion effects can be corrected computationally. We propose an autofocus algorithm that utilizes our previous research[1] for automatic and reliable estimation of the dispersion parameters of the delay line and the medium and applies these parameters to produce a corrected image. This autofocus algorithm is suitable for implementation on a digital-signal-processor-based OCT system for rapid, real-time correction of images.

Dispersion is a linear effect in which the group velocity in a medium depends sensitively on the wavelength of light. The effect of dispersion on OCT imaging is that previously sharp features are blurred into adjacent features, resulting in a reduction of image quality. A similar effect is observed on a photograph that is taken out of focus. However, there is an important difference between these two situations. In the case of a blurry photograph, information is lost because high spatial frequencies are not transmitted through the optical system. Dispersion in OCT, however, does not degrade the power spectrum of the collected signal whatsoever. As a result, dispersion in OCT can be corrected digitally without any image-quality consequences.

Both digital and optical methods have been utilized to correct dispersion in OCT images. Fercher *et al.*[2] utilized a space-variant convolution kernel to deconvolve depth-dependent dispersion. Optical phase conjugation methods, such as employed by Drexler *et al.*[3] insert various transparent optical materials to balance the dispersion between the reference and the signal arm of the interferometer. Another method has processed data in the Fourier domain to remove defects.[4] Also, a CLEAN-type algorithm[5] can identify dispersed pointlike scatterers in tissue. Potentially, the contrast criterion we utilize could be used in conjunction with another dispersion compensation method to achieve an alternate autofocus method.

Biological tissues generally contain a wide variety of materials, each of which has different dispersion properties. It is desirable for a medical instrument to automatically adapt to the tissue by calibrating the dispersion parameters without a separate measurement. By introducing a compensating dispersion into the delay arm, the image can be corrected in the optical system. However, digital processing adds a high degree of flexibility, as well as eliminates the complexity of optical dispersion compensation. Modern digital signal processors provide the capacity for real-time correction of the image, so that optical compensation is not required. In addition, digital filters can also compensate for spectral nonuniformity and reject noise at the same time. We believe that for these reasons digital analysis will become an integral and necessary part of an OCT instrument.

2. Algorithm Description

Any automatic algorithm, such as blind deconvolution algorithms, must make *a priori* assumptions about the nature of the distortion and the image. For typical image restoration, one can stipulate that the unblurred image be positive valued, as well as the blurring function. Also, other assumptions can be made about finite support when the image is surrounded by a dark area. Unfortunately, we cannot make these assumptions because, in general, the OCT reflectance data can take on positive or negative values. This reflectance can be of either sign because positive reflections occur at higher-to-lower refractive-index boundaries while negative reflections occur at the surface of conductors or at lower-to-higher refractive index boundaries. The sign of the reflectance corresponds to a phase shift of 0 or π in the measured interferogram of a reflector relative to the reference signal. The nature of dispersion is that it is a power-preserving phase distortion, not a convolution of intensities, which, in general, means that any chirped reflectance function can plausibly be caused by a chirped set of reflectors that are distributed in the medium by frequency. However, most biological tissues do not contain objects where periodic structures of different periods are spatially separated. Most structures are characterized by speckle objects that lack any long-range correlations in the distributions of reflectors in the tissue. We note, however, that almost any set of chirp parameters can produce a plausible estimate of the reflectors. We have chosen a method that empirically produces good results on specklelike objects.

Many, but not all, biological structures possess features with contrast and sharp boundaries. This aspect becomes especially true as the bandwidth increases and one can resolve individual cells and their constituents. A human operator attempting to guess the right chirp parameters might adjust the parameters to achieve a sharp-looking object with narrow boundaries. Our algorithm is essentially an automated way to do this. The method is to design a functional for the OCT reflectance data, adjusted with trial dispersion parameters, that tends to be minimized when the adjusted data contains sharp boundaries and objects. We then optimize this functional over the dispersion parameters. Since the number of dispersion parameters is usually fairly low, and this functional tends to be globally smooth with relatively weak cross dependence of the parameters, this optimization converges quickly. These parameters can then be typically applied globally to the OCT image if the material composition in each axial scan is similar.

For a complete review of the formalism used here, we refer the reader back to our earlier research.[1] We assume that one has applied the algorithm to the point where one has computed $\tilde{G}(\omega)$, the Fourier transform of the temporal reflectance function of the axial scan. This result should ideally already have the noise filtered out, perhaps by use of the Wiener-type filter presented in our previous research. Because of dispersion, this result does not directly correspond to the spatial features in the reflectance. Dispersion compensation uses knowledge of the material dispersion to compute the actual reflectance function $g(z)$ from $\tilde{G}(\omega)$. We will constrain the reflectance function to be nonzero only for $z > 0$. The functional Λ computed from a trial reflectance function $g(z)$ will be

$$\Lambda = -\int_0^\infty |g(z)|^{2(1+\gamma)}\mathrm{d}z. \tag{1}$$

This functional has several properties that make it attractive for finding sharp boundaries. First, since it integrates over the entire reflectance function, there is no preference on the actual position or permutations of the reconstructed data. Second, this function is always negative, so that an upper bound is always known. Finally, the reflectance depends only on $|g(z)|^2$, the energy in the reflectance signal at each position (and disregards phase). The total energy in the signal is invariant to charges in the chirp parameters, which corresponds to setting $\gamma = 0$. (As a result, $\gamma = 0$ is not a useful value for optimization of Λ.) Values of $\gamma > 0$ will tailor Λ to decrease when pointlike objects are present in the signal, emphasizing sharp features. Conversely, for $\gamma < 0$ the signal tends to be smoothed out. We will use values of $\gamma > 0$ for this functional to sharpen boundaries. In particular, the value of $\gamma = 1$ may offer computational convenience by allowing one to perform the squaring operation twice rather than resort to an exponent operation.

By choosing γ, we can control the global smoothness of the functional Λ. Large values of γ tend to produce sharply peaked values of Λ, whereas values near zero tend to smooth out Λ. When one optimizes Λ, a low value of γ can be chosen to provide a gentle push toward the minimum when attempting to find the global minimum, whereas high values of γ can be used when one wants to quickly find the local minimum. We have found that the dispersion parameters that minimize Λ are insensitive to the actual

value of γ chosen, so changing the parameter during optimization does not compromise the eventual target parameters. Although Eq. (1) has an analytic derivative, we recommend against using gradient information of Λ during optimization because although Λ is typically globally smooth, it often has small, high-frequency ripples that make gradient information less useful.

The functional of Eq. (1) has a relation to the minimum entropy method. When γ is near zero, Λ can be approximated by a Taylor series in γ. The constant term of this series is the energy of the signal, which is invariant to changes in the dispersion parameters. The magnitude of the first-order term is given by its first derivative:

$$\frac{d\Lambda}{d\gamma}\bigg|_{\gamma=0} = -\int_0^\infty |g(z)|^2 \log[|g(z)|^2]dz. \quad (2)$$

This function is the definition of Shannon entropy[6] for the distribution $|g(z)|^2$, if the energy in the signal is normalized to 1. In the maximum entropy method, this functional would be maximized to spread the power out over the image as widely as possible, constrained by a goodness of fit to the data. In this case, we minimize it to create as sharp of a reconstruction as possible, because it is possible to blur out the data arbitrarily with large chirp parameters. This autofocus algorithm can be considered to be a minimum entropy algorithm that minimizes the Renyi entropy,[7] which approaches Shannon entropy in the limit of $\gamma \to 0$.[6] Another application of Renyi entropy minimization to blind source separation can be found in Ref. 8.

Sets of dispersion parameters generally fall into two categories: fixed dispersion and material dispersion. Fixed dispersion can be measured if one places a mirror at the location of the top surface of the sample. Since the mirror produces no dispersion, the signal contains only the information about the dispersion of the delay system at that position. With a sample, the dispersion in the sample is due to the delay system dispersion plus the total material dispersion at a given depth. Depending on the degree of dispersion correction required, one can correct only the fixed dispersion, or both the fixed and the material dispersion. For wide bandwidth sources and long axial-scan ranges, material dispersion compensation is typically necessary.

Rather than an integral formation, we develop the algorithm in a unitless discrete-time formation that is much more likely to be useful in practice. Because all the dimensionality of the quantities will be removed, the algorithm is scaled to the sampling rate of the delay line. The formulas presented assume that the maximum frequency of all of the spectra is ω_{max}.

3. Algorithm Discrete-Time Implementation

We assume that we have sampled the complex Fourier spectrum of the samples of an axial scan. We call these samples $\tilde{G}_n$ where n is an integer between 0 and $N - 1$. For an ideal delay line, we compute the discrete Fourier transform (DFT) $\tilde{F}_n$ from the N samples of the interference signal f_j:

$$\tilde{F}_n = \sum_{j=0}^{N-1} f_j \exp\left(\frac{\pi i j n}{N}\right). \quad (3)$$

This DFT is usually implemented with the real-to-complex fast Fourier transform (FFT) algorithm, with the original signal f_j padded with N zeros. If the delay line is not ideal, a discrete version of the procedure in Ref. 1 should be used. We also assume we know the discrete power spectrum of the source $\tilde{S}_n$. We have found that $\tilde{S}_n$ can be estimated from the image itself by averaging together the magnitude of the DFT $|\tilde{F}_n|$ of all the axial scans in a two-dimensional image. Since this estimate will have a few ripples due to the placement of scatterers on an axial-scan line, it helps to smooth the spectrum by convolving it with a positive-valued filter. Since most sources produce relatively slowly varying spectra, this usually does not affect the estimate significantly except to remove these ripples.

A useful optimization after the DFT is performed is to extract only the portion of the spectrum known to contain wavelengths that are actually present in the source. This extraction prevents a resampling over a much more densely sampled function than needed, minimizing the computational burden. If the magnitude of $g(z)$ is displayed, the image produced will be invariant to scale changes or translations in the Fourier domain. The only difference is a change in the carrier frequency of the reconstruction. We will assume that this operation has been done so that the fractional bandwidth of the extracted signal is on the order of 1.

The spectral estimate $\tilde{S}_n$ contains the sum of the source spectrum and the noise spectrum. The noise spectrum usually has a relatively constant power spectral density. We can estimate the noise spectrum by averaging the power spectral density of S_n over a region of the Fourier spectrum that is outside of the source spectrum. We call this estimate N_0. We can then use the Weiner filter estimate to compute $\tilde{G}_n$:

$$\tilde{G}_n = \frac{\tilde{F}_n \max(\tilde{S}_n - N_0, 0)}{\max(\tilde{S}_n - N_0, 0)^2 + N_0^2}. \quad (4)$$

The function max gives the largest value of its arguments. One may want to multiply N_0 by a small constant to produce a slightly pessimistic noise estimate that will ensure that all frequencies not emitted by the source make no contribution to the reconstruction.

Another value that must be determined is ω_{ctr}, which is the scaled centroid of the spectrum of S_n:

$$\omega_{ctr} = \frac{\sum_{n=0}^{N-1} n \max(\tilde{S}_n - N_0, 0)}{\sum_{n=0}^{N-1} N \max(\tilde{S}_n - N_0, 0)}. \quad (5)$$

Now that $\tilde{G}_n$ and ω_{ctr} are known, we can attempt to apply operations that remove the dispersion. To remove fixed dispersion, we define the dispersion parameters α_2 and α_3 as correcting second- and third-order dispersion, respectively. We form the estimate of the corrected spectrum $\tilde{G}_n'$ by means of

$$\tilde{G}_n' = \tilde{G}_n \exp\left[i\pi\alpha_2\left(\frac{n}{N} - \omega_{ctr}\right)^2 + i\pi\alpha_3\left(\frac{n}{N} - \omega_{ctr}\right)^3 \right].$$
(6)

Expressed in this way, the maximum magnitude of α_2 before aliasing occurs is $N/2$. In general the maximum magnitude for α_n is N/n. Therefore, the search for the correct value of α_n is confined to this range.

If desired, one can correct the material dispersion by resampling the Fourier spectrum from ω to k space. Because we are manipulating a sampled Fourier spectrum, it is desirable to maintain the same sampling rate in the discrete k variable as the ω variable so that the k sampling does not oversample or undersample the modified Fourier spectrum. To resample $\tilde{G}_n'$, we produce an array of indices into $\tilde{G}_n'$ called i_n, which determine the points of $\tilde{G}_n'$ that are to be resampled. The resampled array is called $\tilde{G}_n''$. We define two material dispersion parameters β_2 and β_3 that correct second- and third-order material dispersion, respectively. The resampling array i_n is given by means of

$$i_n = n + \beta_2\left(\frac{n}{N} - \omega_{ctr}\right)^2 + \beta_3\left(\frac{n}{N} - \omega_{ctr}\right)^3.$$
(7)

Given this form of i_n, the maximum values of β_2 and β_3 to prevent aliasing are approximately $N/2$ and $N/3$, respectively. Using a standard sinc-type interpolator, the array $\tilde{G}_n''$ can be computed from $\tilde{G}_n'$ by means of

$$\tilde{G}_n'' = (i_{n+1} - i_n) \sum_{j=0}^{N-1} \tilde{G}_j' \frac{\sin[\pi(j - i_n)]}{\pi(j - i_n)}.$$
(8)

The factor $(i_{n+1} - i_n)$ is an important Jacobian-type rescaling factor to maintain the same energy in the reconstructed signal. Although we have shown a sinc-type interpolator, we recommend a windowed sinc interpolator such as the prolate-spheroidal interpolator[9] because of its improved convergence properties. Once $\tilde{G}_n''$ is found, the inverse DFT can be used to compute the estimate of g_n, the sampled version of the dispersion-corrected axial scan (n from 0 to $N - 1$):

$$g_n = \frac{1}{N} \sum_{j=0}^{N-1} \tilde{G}_j'' \exp\left(\frac{-\pi i j n}{N}\right).$$
(9)

One can accomplish this DFT by zero padding the samples of $\tilde{G}_n''$ with N zeros and taking the inverse FFT. If the complex-to-real inverse FFT is used, one will not have the benefit of getting the complex analytic extension of g_n. The analytic extension is use-

ful because, as we pointed out in our earlier paper,[1] the magnitude $|g_n|$ can be a useful estimate of the scattering amplitude in the presence of speckle.

4. Optimization of the Functional over the Dispersion Parameters

With the dispersion parameters already known, Section 3 provides a recipe for recovering undistorted axial-scan reflectance data. We now outline a procedure in which we can use this to search for the dispersion parameters that optimize the functional of Eq. (1). Essentially, this method is an adaptation of the bracketing and golden section search procedure.[10] The golden-section search is a method that iteratively subdivides an interval in which a maximum or minimum is known to exist until it is isolated to a desired accuracy. It is called golden section because the ratio between the widths of the two subdivided intervals is given by the golden ratio. Because of this, the golden-section search is very robust but only provides linear convergence. Because of the roughness of the functional on the small scale, it is desirable to avoid using gradient-based search techniques, but other curve-fitting techniques such as Brent's method may improve convergence.[10]

To use an optimization search algorithm requires that a region of the domain of the function be established to contain a minimum. One establishes this region by bracketing a minimum, which entails identifying two end points of an interval and a point in between that has a smaller value than the end points. This initial step is often more difficult and time consuming than the actual optimization search because in general there may be little information about the actual location of the maximum. In the Section 3, we established limits on the magnitude of the parameters α_2, α_3, β_2, and β_3. A useful lower limit estimate of the magnitude of these parameters is usually given by 1, because parameters with less than this magnitude tend to provide little noticeable correction.

In this algorithm, we will assume that there is an nonscattering region in the axial scan above the surface of the biological tissue. The presence of such a region is frequently the case when the tissue is surrounded by a transparent medium (e.g., water or air). Because dispersion tends to blur features on the axial scan, the correct dispersion parameters are likely to make the boundary between the transparent medium as sharp as possible. By attempting to find the dispersion parameters that optimize the entropy at the boundary, we may cancel the effects of dispersion in the delay line at the tissue boundary. We will assume that the uncorrected axial-scan Fourier spectrum $\tilde{G}_n$ has been determined, for example, from Eq. (4). We then compute an uncorrected axial-scan reflectance g_n from it by using a DFT such as Eq. (9). Even with dispersion, the initial reflection on the axial scan is usually readily recognizable. Assume the front reflection has been determined to start at sample number m on the axial scan, and end at po-

sition m'. We create two new arrays g' and h from this data:

$$g_n' = g_{n+m}, \qquad \text{for } n < N - m,$$

$$g_n' = 0, \qquad \text{otherwise},$$

$$h_n = g_{n+m}, \qquad \text{for } n < m' - m. \tag{10}$$

The array g_n' is the axial-scan data with the empty space removed, whereas the array h_n is an array of length $m' - m$ just representing the initial reflection on the line. The task is to find the fixed dispersion parameters α_2 and α_3. One obtains these parameters by finding the minimum value of the functional Λ over α_2 and α_3 as applied to the initial reflection h_n:

$$\Lambda_h = -\sum_{n=0}^{m'-m-1} |h_n|^{2(1+\gamma)}. \tag{11}$$

The task is to determine the value of α_2 that minimizes Λ_h. We first recompute the Fourier spectrum $\tilde{H}_n$ using the DFT as in Eq. (3). Next, we bracket a minimum of Λ_h. We assume that the magnitude of α_2 lies within $\epsilon N/2$ to $N/2$, where ϵ is a small nonzero number (usually $\epsilon = 1/N$ suffices). The bracketing procedure is to form a sequence of M trial intervals in α_2 that we note by $\alpha_n' = N\epsilon^{(M-n)/M}/2$. We then compute $\Lambda_h(\alpha_n')$ and $\Lambda_h(-\alpha_n')$ for each value of α_n'. Note that we compute both positive and negative values because we are searching in both directions. One computes the values by using Eq. (6) applied to $\tilde{H}_n$, using the inverse DFT of Eq. (9) to compute the trial h_n, and then performing the sum of Eq. (11). When these formulas are used, the length N should be replaced by the new length $m' - m$. One can then bracket the minimum by finding the value of α_n' or $-\alpha_n'$ with the smallest value of $\Lambda_h(\pm\alpha_n')$ that is also smaller than $\Lambda_h(\pm\alpha_{n\mp1})$ and $\Lambda_h(\pm\alpha_{n\pm1}')$. The values of α_{n-1}', α_n', and α_{n+1}' will then bracket the minimum if M is sufficiently large. Once the minimum is bracketed, the golden-section search can be used to hunt for the minimum value of $\Lambda_h(\alpha_2)$ in the bracketed interval. The described procedure is a straightforward application of the golden section algorithm to the function $\Lambda_h(\alpha_2)$.

Once the minimum value of α_2 is found, one can search for the minimum value of $\Lambda_h(\alpha_3)$ over the dispersion parameter α_3. The previous value of α_2 should be used from the earlier step in Eq. (6) but should be left fixed during the optimization of α_3. A similar procedure can be used to bracket the minimum of α_3 somewhere between $\epsilon N/3$ and $N/3$ and then to find the minimum through a golden-section search method. If desired, one can then go back and refine the value of α_2 using the value of α_3 and iterate until convergence, if that level of accuracy is required.

The optimal values of α_2 and α_3 should be used to correct the signal g_n' as defined in Eq. (10). One performs this correction by taking the DFT of g_n' and applying Eq. (6) to find $\tilde{G}_n'$. It is important to use g_n' rather than g_n because the stationary point at which no material dispersion correction is applied is

at the beginning of the line, and this reflection has already been well corrected and should not be further altered.

A similar procedure is used to find the parameters β_2 and β_3. We form the sequence of M trial intervals $\beta_n = N\epsilon^{(M-n)/M}/2$. Computing the values of Λ_h for each β_n allows the minimum to be bracketed if a large enough value of M is chosen. One calculates each value of Λ_h by taking the corrected $\tilde{G}_n'$ and applying the resampling of Eqs. (7) and (8). The corrected dispersion data is calculated with the DFT of Eq. (9), and Λ_h is computed from the corrected data with Eq. (11). Once the minimum is bracketed, a golden-section search narrows the bracketed interval. First the value of β_2 can be optimized, leaving $\beta_3 = 0$. Then β_3 is optimized. Again, one can go back and improve the value of β_2 through further iteration.

There is one case in which the dispersion parameters may be difficult to determine with this method. When looking at a periodic object, there are multiple values of the dispersion parameters that have identical maxima. Identical maxima are present because of a Talbot effect,[11] but occurs in the time domain rather than the spatial domain. The spatial Talbot effect occurs when a periodic field diffracts through space and reproduces itself identically in a periodic manner. Similarly, with a periodic structure, there are multiple values of the second-order dispersion that are equally spaced and that reproduce the unchirped structure. This structure may not significantly affect the reconstruction of periodic structures, but layers beneath them will have an incorrect correction, resulting in a blurred reconstruction. Some structures, such as the retinal nerve fiber layer or muscle fibers may be somewhat periodic, and therefore one must consider the possibility that there may be many local minima during optimization of Λ_h over α_2 and β_2.

Another important note is that there is an equivalence between fixed and material dispersion over translation of the axial scan. If the axial scan is translated in the spatial domain by d samples, then the values of α_2 and α_3 need to be changed to compensate for the fact that the amount of dispersion applied by the resampling process in Eq. (8) depends on where on the axial scan the reflectance resides. One encounters this equivalence by comparing the effects of Eqs. (6) and (7) when the object is a point reflector placed at a position d, which has an unmodified reflectance function $\tilde{G}_n = \exp(i\pi dn/N)$. If the parameters α_2^{old}, α_3^{old}, β_2, and β_3 correct the axial scan given by the signal g_n, the new parameters to correct a translated axial scan $g_n' = g_{n-d}$ will be

$$\alpha_2^{\text{new}} = \alpha_2^{\text{old}} - \beta_2 d/N,$$

$$\alpha_3^{\text{new}} = \alpha_3^{\text{old}} - \beta_3 d/N. \tag{12}$$

5. Experimental Performance

The ultimate utility of a method intended to simplify the practical application of an art can be proved only in the field. However, as an example we show the
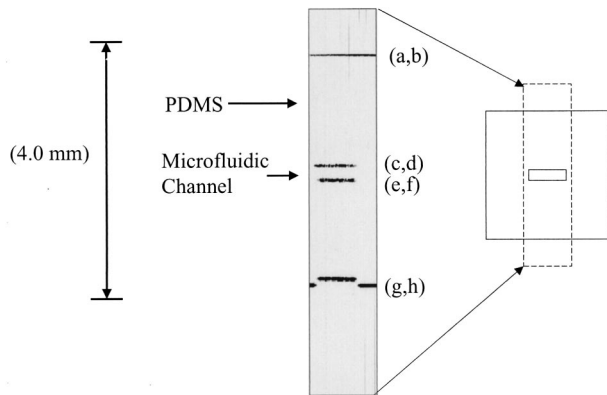
Fig. 1. Low-resolution OCT image of the PDMS microfluidic structure with a schematic of the cross section of the microfluidic channel.

Fig. 2. Source spectrum and digitally modified spectrum.

application of the algorithm to two test objects: a microfluidic structure and a tadpole. The microfluidic structure in a polydimethylsiloxane (PDMS) polymer contains simple reflective layers so that the boundary reflections can be examined in detail, whereas the tadpole is included as an example of enhancement of biological imaging.

Our OCT system consisted of a passively mode-locked, Ti:sapphire laser with a center wavelength of 800 nm generating 100-fs pulses at a rate of 80 MHz with 500-mW average power. By sending the pulses through a narrow-core high-index silica–germania fiber, these were broadened through nonlinear continuum generation[12] to an approximately 80-nm FWHM bandwidth between 760 and 840 nm. The OCT system was implemented as a Michelson interferometer utilizing fiber-optic waveguides, a galvanometer-scanned retroreflecting mirror as the delay line, and galvanometer-scanned mirrors to steer the beam in the transverse direction in the sample. With the bandwidth used, dispersion is noticeable in the PDMS for scan depths larger than a millimeter. Imaging the microfluidic structure in PDMS required use of a 50-mm, focal-length visible-wavelength achromatic doublet lens because a long depth of field was necessary to simultaneously image the top and the bottom surfaces of the microfluidic device. Because of the large thickness of the achromat (approximately 7 mm), it produced most of the dispersion that was encountered in the axial scan. However, the PDMS itself also produced enough dispersion so that correction of the dispersion of the achromat was insufficient to achieve bandwidth-limited imaging performance at all depths. Figure 1 shows a low-resolution image of the PDMS microfluidic device. Four air–PDMS surfaces are in this device, two of which are the exterior top and bottom surfaces [the surfaces marked (a, b) and (g, h)] and two of which are formed by an interior channel in the microfluidic [marked by (c, d) and (e, f)].

The interference data was acquired for each axial scan, with 200,000 samples per scan digitized to 12-
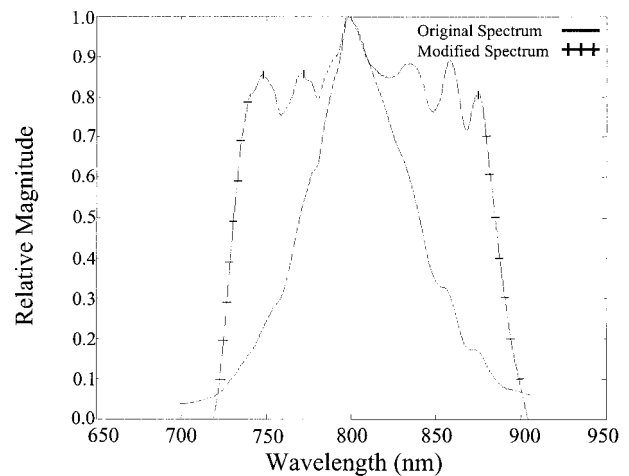
bits resolution. The first task was to estimate the power spectral density of the laser and the noise spectrum magnitude. To do this, the FFT was taken of all of the scan lines in the image, and the magnitudes of these were averaged together. This estimate was then blurred by use of a 10-nm-wide filter to remove oscillations in the spectrum that occur due to the regular placement of layers in the PDMS (this regularity does not typically occur in biological samples). From the magnitude of the spectrum in the visible-wavelength band (where no light was emitted by the laser), the noise power spectral density was estimated. Figure 2 shows the original spectrum (solid curve), and the modified spectrum (hatched curve) with the Weiner filter applied to the spectrum. Since the sample was illuminated with approximately 20 mW of power, the shot noise was low, and therefore much more bandwidth could be extrapolated from the signal.

The center scan line was utilized for the autofocus algorithm. The interference pattern from the top reflection was isolated, and the golden-section search method was utilized to minimize the Renyi entropy over the fixed dispersion parameters α_2 and α_3. The quadratic entropy was used, so $\gamma = 1$ in the entropy computation of Eq. (1). Once these parameters were found, the entire axial scan was corrected, so that the remaining dispersion was due to the PDMS only. Then, the golden-section search was used to minimize the Renyi entropy by use of the material dispersion parameters β_2 and β_3 over the entire axial-scan line. The resultant parameters were used to correct the entire axial scan. The original and corrected interference data are shown in Fig. 3. The original reflections in the microfluidic corresponding to the top PDMS–air surface, top air–PDMS surface inside the channel, bottom PDMS–air surface inside the channel, and bottom air–PDMS surface are shown in the temporal interferograms (a, b), (c, d), (e, f), and (g, h) respectively. The letters (a, c, e, and g) correspond to the original interferograms, whereas the letters (b, d, f, and h) correspond to the dispersion-corrected
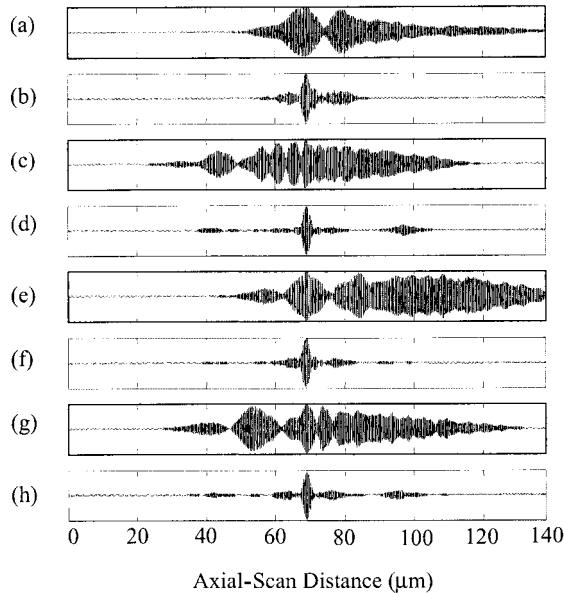
Fig. 3. Autofocus digitally corrected reflections off of interfaces of microfluidic structure. Plots (a), (c), (e), and (g) correspond to the uncorrected reflectance functions, whereas (b), (d), (f), and (h) are the corrected point-spread functions.

interferograms. The FWHM of the corrected interferograms achieves nearly the bandwidth-limited performance of approximately 2 μm at all four depths. The minimization of Renyi entropy serves to maximize the peak energy of the reflections, which concentrates the energy as much as possible in the four reflections.

The other autofocus example is from a *Xenopus laevis* (African frog) tadpole, which has an internal structure not nearly as well controlled as the PDMS microfluidic, but is a more realistic test of the algorithm. The tadpole specimen was cared for and handled under the approved protocols of the University of Illinois at Urbana-Champaign Committee on Animal Care. We anesthetized the tadpole by immersing it in a 0.05% solution of tricaine until the specimen no longer responded to touch. The specimen was placed on the stage of our OCT instrument for imaging. A 20-mm, focal-length, 6-mm-diameter, infrared achromat was utilized as the focusing objective, resulting in far less delay-line dispersion. The spot size is approximately 10 μm, whereas the axial coherence length is approximately 2 μm. The spectrum of the illumination was very similar to that shown in Fig. 2. Figure 4 shows an image of a section of a live tadpole, without [4(a)] and with [4(b)] correction. For each image, we show the same expanded section. The points, which are blurred in the axial direction in image 4(a), appear as compressed points in image 4(b) because the axial resolution is much better than the transverse. Figure 5 shows an expanded version of pointlike objects (cell nuclei) from four different depths in the tadpole image before and after autofocus correction. The objects appear much sharper and well defined owing to the decrease of axial blurring.

Finally, Fig. 6 shows the dependence of the quadratic Renyi entropy on the delay-line chirp parameter α_2 and the material dispersion parameter β_2. This entropy is computed for the 200th scan line, which was used in Fig. 4 to optimize the autofocus dispersion parameters. The vertical axis is inverted so that the minimum appears as a peak. There is a clear, sharp peak in the delay-line entropy α_2 that corrects much of the dispersion in the axial scan line. At this bandwidth and axial-scan range, most of the blurring occurs because of the delay-line dispersion and therefore is primarily corrected by the choice of α_2. A somewhat more modest but still noticeable correction is achieved in optimizing the Renyi entropy over the parameter β_2. These two chirp parameters correspond to a total blurring at the surface of 10 μm and a blurring of 25 μm at a depth of 1 mm. Since the bandwidth-limited resolution is approxi-
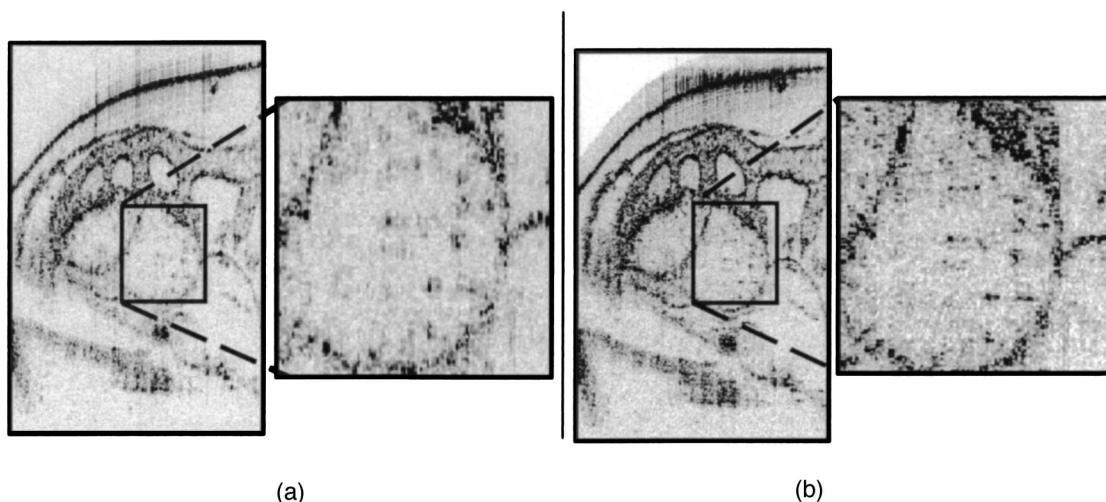

(a)   (b)

Fig. 4. Image of a tadpole: (a) before automatic dispersion correction and (b) after automatic dispersion correction. The boxes to the right of each image show an expanded version of each image.

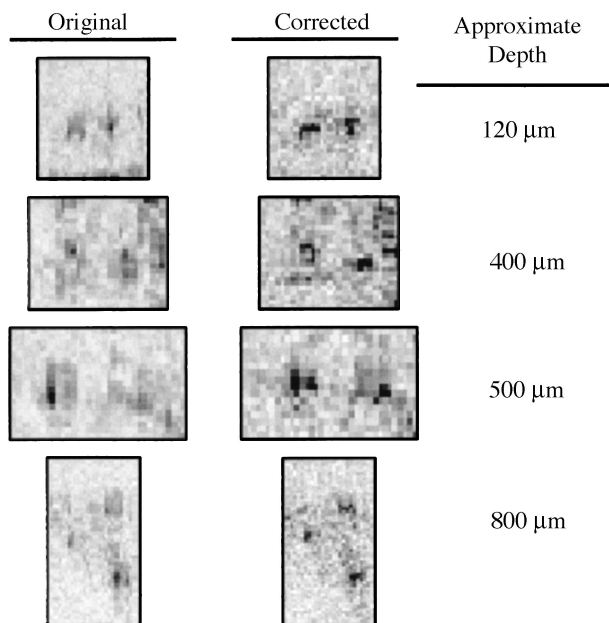| Original	Corrected	Approximate Depth
		120 μm
		400 μm
		500 μm
		800 μm

Fig. 5. Four sections of pointlike objects (cell nuclei) from the tadpole images, taken at different depths in the image, and their corrected versions.

mately 2 μm, the autofocus algorithm results in a significant improvement in resolution that would be degraded by dispersion.

6. Discussion and Conclusion

Ideally, an image-enhancement algorithm would have a model of the image type it is attempting to restore so that the algorithm could achieve the best possible restored image. However, image characteristics of biological tissues vary widely, and such a model would be difficult to construct. In incoherent microscopy, sharpness of the image can only occur when the object is in focus. However, dispersion in coherent imaging causes interference between adjacent features; thus dispersed features can still potentially have bright points. Despite this fact, an autofocus algorithm can be implemented when the distribution of energy of an axial scan is concentrated by minimization of the Renyi entropy. Using a relatively simple criterion, one can find the scattering amplitude inside tissue, accounting for dispersive ef-
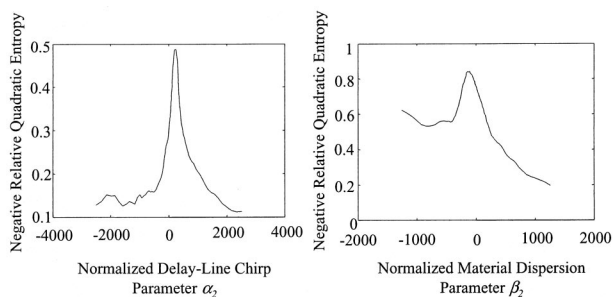

Fig. 6. Dependence of Renyi quadratic entropy ($\gamma = 1$) on the chirp parameters α_2 and β_2.

fects. Since most tissues do not have long-range order or periodic structures, Talbot-type multiple minima to the Renyi entropy are not likely to occur in practice.

The autofocus algorithm that we have described is a scalar algorithm and therefore does not account for polarization effects such as polarization-mode dispersion. Much biological media consists of isotropic materials and therefore will not significantly exhibit this effect. However, some fibrous structures such as muscle and nerve fibers have form birefringence, and the crystalline lens of the eye also exhibits birefringence. At any depth in the tissue there can be a group delay associated with both polarization modes. Because both modes will likely project onto the measured intensity signal, one may observe both polarization modes coherently superimposed on the axial-scan data. Rather than being described by a single scalar dispersion function, it is possible to characterize the medium with a wavelength-dependent dielectric tensor. However, characterization of the medium in this manner means that polarization-sensitive OCT must be used to capture the interference, and four parameters must be fit to the medium (if it is assumed lossless). Fitting these parameters adds significant complication to the algorithm. However, correcting for the average dispersion of both polarizations will likely still improve the image even if polarization effects are not considered.

We have demonstrated an autofocus algorithm to automatically compensate for dispersive effects in media by utilizing our previously described dispersion compensation method in conjunction with an entropy optimization method. In this method we are fitting only one set of parameters for the entire medium. Therefore, our parameters will necessarily average out the effects of varying material composition. However, because biological tissues tend to contain mostly water, hemoglobin, and lipids as their primary constituents, it is likely that the assumption of a single medium will result in a superior reconstruction, compared with that from use of no material dispersion compensation. Corrected images of a PDMS microfluidic device, which has a known composition, and a tadpole have significantly improved contrast and resolution owing to the average material dispersion correction. The flexibility of digital interferogram processing permits an essentially arbitrary transformation to the image. Because dispersion does not result in a degradation in the power of the captured signal, there is no noise penalty for performing the correction digitally. For this reason we believe that digital signal processing will become an indispensable part of OCT, as it has become for other three-dimensional imaging modalities.

References

1. D. L. Marks, A. L. Oldenburg, J. J. Reynolds, and S. A. Boppart, "Digital algorithm for dispersion correction in optical coherence tomography for homogeneous and stratified media," Appl. Opt. **42,** 204–217 (2003).

2. A. F. Fercher, C. K. Hitzenberger, M. Sticker, R. Zawadzki, B. Karamata, and T. Lasser, "Numerical dispersion compensation for Partial Coherence Interferometry and Optical Coherence Tomography," Opt. Express **9,** 610–615 (2001), http://www.opticsexpress.org.

3. W. Drexler, U. Morgner, F. X. Kartner, C. Pitris, S. A. Boppart, X. Li, E. P. Ippen, and J. G. Fujimoto, "*In vivo* ultrahigh resolution optical coherence tomography," Opt. Lett. **24,** 1221–1223 (1999).

4. K. M. Yung, S. L. Lee, and J. M. Schmitt, "Phase-domain processing of optical coherence tomography images," J. Biomed. Opt. **4,** 125–136 (1999).

5. J. M. Schmitt, "Restoration of optical coherence images of living tissue using the clean algorithm," J. Biomed. Opt. **3,** 66–75 (1998).

6. T. M. Cover and J. A. Thomas, *Elements of Information Theory* (Wiley, New York, 1991).

7. A. Renyi, *Probability Theory* (North-Holland, Amsterdam, Netherlands, 1970).

8. E. Kenneth, I. Hild, D. Erdogmus, and J. C. Principe, "Blind source separation using Renyi's Mutual Information," IEEE Signal Proc. Lett. **8,** 174–176 (2001).

9. J. J. Knab, "Interpolation of band-limited functions using the approximate prolate series," IEEE Trans. Inf. Theory **IT-25,** 717–720 (1979).

10. W. H. Press, S. A. Teukolsky, W. T. Vetterling, and B. P. Flannery, *Numerical Recipes in C* (Cambridge University Press, Cambridge, U.K., 1988).

11. J. Goodman, *Introduction to Fourier Optics* (McGraw-Hill, New York, 1968).

12. D. L. Marks, A. L. Oldenburg, J. J. Reynolds, and S. A. Boppart, "Study of an ultrahigh-numerical-aperture fiber continuum generation source for optical coherence tomography," Opt. Lett. **27,** 2010–2012 (2002).